FAST-TRACK PAPER

The non-geometric $\bar{P}S$ wave in high-resolution seismic data: observations and modelling

Michael Roth and Klaus Holliger

Institute of Geophysics, ETH-Hönggerberg, 8093 Zürich, Switzerland, E-mail: mike@aug.ig.erdw.ethz.ch

SUMMARY

In data from a high-resolution seismic survey conducted over a near-surface environment consisting of homogeneous soft clay, we consistently observe a distinct seismic phase arriving between the direct compressional wave and the Rayleigh wave. This phase is characterized by high amplitudes at near offsets and a phase velocity corresponding to about twice the shear wave velocity. Based on analytical and numerical analyses, this signal could be unambiguously identified as a non-geometric wave, which is excited if the source is located near the Earth's surface and the Poisson's ratio in the vicinity of the source is unusually high. To date there are only a few speculative observations of this particular non-geometric seismic wave phenomenon. However, given the commonly very high Poisson's ratio of surficial materials, we expect this phase to be present, albeit unidentified, in many near-surface seismic surveys. The presence of this non-geometric wave increases the complexity of the seismic record, and failure to identify it may result in misinterpretations, particularly of high-resolution seismic reflection data as well as of shear wave and surface wave data. Potential applications of this seismic phase may arise from its high sensitivity to the shear wave velocity in the immediate source region.

Key words: exploration seismology, Poisson's ratio, seismic modelling, seismic phase identification, seismic wave propagation.

1 INTRODUCTION

The shallow subsurface typically consists of unconsolidated sediments characterized by very high ratios of compressional (P) to shear (S) wave velocities (Stümpel *et al.* 1984). A typical seismic record from such an environment is dominated by the direct compressional wave, often followed by a coherent train of guided waves, and the Rayleigh wave train. Shallow seismic reflections are observed in the time-offset window bounded by the direct P wave and the Rayleigh waves (Robertsson *et al.* 1996). Fig. 1 shows two typical trace-normalized shot gathers collected over a near-surface environment consisting predominantly of soft and relatively homogeneous lacustrine clay. We used a shotgun fired at about 1 m depth as a seismic source and recorded the signals with 30 Hz vertical geophones. Receiver spacing was 1 m and the profile length was 40 m. We observe the direct P wave arriving with a phase velocity α of about 1500 m s^{-1} and Rayleigh waves with a phase velocity v_R of about 100–110 m s^{-1}. The S-wave velocity of the sediments can thus be estimated from the phase velocity of the Rayleigh waves as $\beta \approx 1.05 v_R = 105–115$ m s^{-1}. This implies an

extraordinarily high Poisson's ratio σ of 0.498. Note that the Poisson's ratios for 'ideal' solids and liquids are 0.25 and 0.50, respectively.

An interesting feature in these seismic records is the prominent seismic phase lying between the P wave and Rayleigh wave arrivals. It has a phase velocity of about 220 m s^{-1}, that is, about twice the value of the S-wave velocity, and fades out at offsets greater than 20 m. This signal cannot be a direct S wave because of its high horizontal phase velocity. It is also unlikely to be a P-wave conversion from structural heterogeneities near the source because its occurrence and amplitude-versus-offset behaviour are similar in each shot gather over the entire survey. We therefore suspect that this phase represents a non-geometric wave generated by the interaction of the seismic source with the free surface. In a homogeneous full space, an explosive seismic source radiates homogeneous (non-decaying) and inhomogeneous (evanescent) P waves. If the source is placed near a seismic discontinuity such as the free surface an inhomogeneous P wave can be transformed into a homogeneous S wave by the reflection. Such wave types are intermediate in character between surface and body waves and are
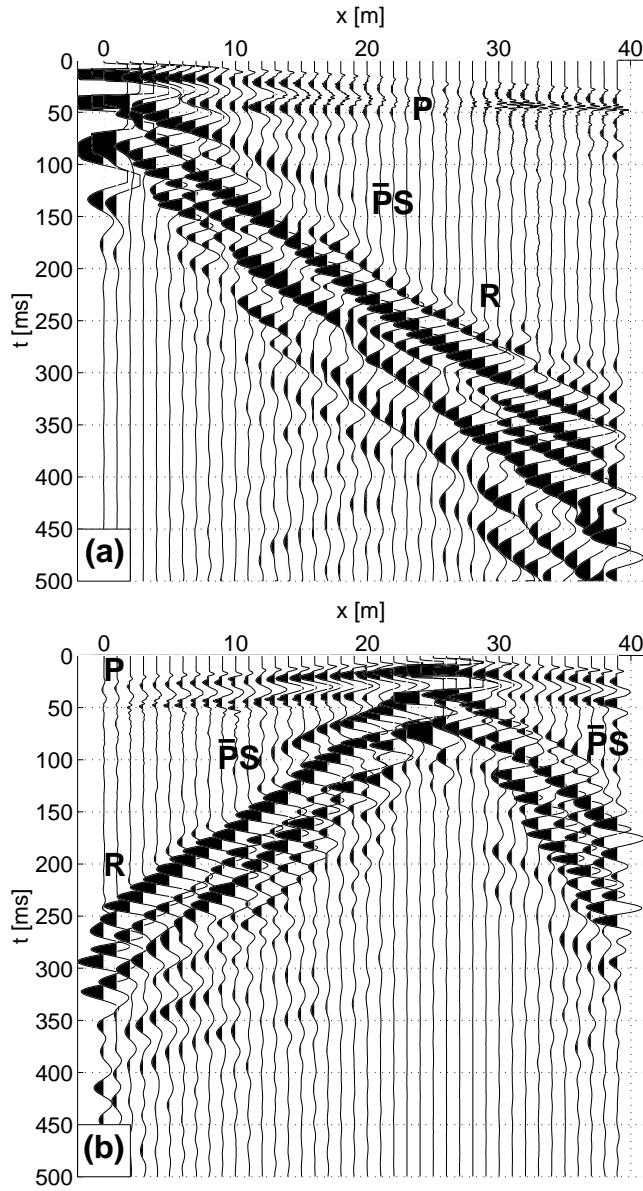
Figure 1. Trace-normalized shot gathers for two source locations: (a) 0.5 m and (b) 25.5 m. *P*: direct *P* wave; *R*: Rayleigh wave; $\bar{P}S$: suspected non-geometric phase.

referred to as non-geometric waves because they are linked to a complex incidence angle and it is not possible to associate them with a geometrical ray path (Kuhn 1985).

Non-geometric waves are well understood theoretically (e.g. Aki & Richards 1980; Brekhovskikh 1980; Tsvankin 1995), but rarely identified in real data. Probably the best-known type of non-geometric wave in exploration seismology is the *S** phase (Hron & Mikhailenko 1981; Fertig 1984; Gutowski *et al.* 1984; Dohr 1985; Lash 1985; Tsvankin 1995). This phase propagates radially with the shear wave velocity from the projection of the source onto the free surface. Usually the *S** phase cannot be observed in surface seismic measurements because at the free surface it interferes with the Rayleigh wave and its amplitude is close to zero. We therefore suspect that the unusual phase in our data corresponds to a rarely observed form of a non-geometric wave characteristic of environments with very

high ratios of *P*-to-*S* velocities. We refer to this wave as $\bar{P}S$ to emphasize its affinity to the geometric *PS* phase. It should, however, be noted that there are different notations for this phase in literature, including '*P̄*-pulse' (Gilbert & Laster 1962; Gilbert *et al.* 1962; Chapman 1972) and '*U*-pulse' (Kuhn 1985). To date we are aware of only a few tentative observations of this particular non-geometric wave (Leet 1949; Kisslinger 1959). The aim of this paper is to identify this phase unambiguously and to characterize its physical properties using both theoretical and numerical methods. We also discuss the relevance of this non-geometric wave for high-resolution seismic surveys in general.

2 INTERACTION OF AN EXPLOSIVE SEISMIC SOURCE WITH THE FREE SURFACE

2.1 Theoretical background

Comprehensive theoretical treatises of non-geometric waves for layered subsurface models are given by e.g. Brekhovskikh (1980) and Tsvankin (1995). For convenience we summarize the key aspects of the theoretical framework of non-geometric waves in a homogeneous half-space in order to clarify the nature and origin of the $\bar{P}S$ phase in our observed data. Our analyses of the interaction of an explosive source with the free surface follow the approach taken by Hron & Mikhailenko (1981) in their study of the *S** phase.

We consider a homogeneous half-space with an isotropic point source located at $x=y=0$ and depth z_0. The wave equation is then given by

$$\frac{\partial^2 \Phi}{\partial t^2} - \alpha^2 \nabla^2 \Phi = 4\pi\alpha^2 f(t)\delta(x)\delta(y)\delta(z-z_0), \tag{1}$$

where Φ denotes the scalar compressional potential, α the phase velocity, δ the Dirac impulse function and $f(t)$ the time dependence of the source. The spherically symmetric harmonic solution of eq. (1) is

$$\Phi(\mathbf{x}, t) = \frac{1}{R}\, e^{i(kR-\omega t)}, \tag{2}$$

with $R = \sqrt{x^2+y^2+(z-z_0)^2}$ being the distance from the source and $k=\omega/\alpha$ the scalar wavenumber (e.g. Aki & Richards 1980). A plane wave representation of the spherical solution is given by Weyl's integral,

$$\frac{1}{R}\, e^{ikR} = \frac{i}{2\pi} \int_{-\infty}^{\infty} \int_{-\infty}^{\infty} \frac{e^{i(k_x x + k_y y + k_z|z-z_0|)}}{k_z}\, dk_x dk_y \tag{3}$$

$$= \frac{ik}{2\pi} \int_0^{\frac{\pi}{2}-i\infty} \int_0^{2\pi} e^{i(k_x x + k_y y + k_z|z-z_0|)} \sin\theta d\theta d\phi. \tag{4}$$

Eqs (3) and (4) are obtained by integrating the Fourier transform of eq. (2) over the vertical wavenumber $k_z = \sqrt{\omega^2/\alpha^2 - k_x^2 - k_y^2}$ and expressing the wavenumbers of the elementary plane waves in terms of their vertical and azimuthal propagation angles θ and ϕ,

$$k_x = k\cos\phi\sin\theta, \quad k_y = k\sin\phi\sin\theta, \quad k_z = k\cos\theta. \tag{5}$$

Weyl's integral is a superposition of homogeneous plane waves propagating in all directions and inhomogeneous plane waves propagating parallel to the *xy*-plane. The inhomogeneous waves have imaginary vertical wavenumbers with $\mathscr{I}\!m\,(k_z) \geq 0$

to satisfy the radiation condition; that is, the amplitude decays in the vertical direction and the angle $\theta = \theta_1 - i\theta_2$ is complex-valued. The integration path for θ in eq. (4) can be subdivided into two parts: the first part follows the real axis from $\theta = 0$ to $\theta = \pi/2$; the second part runs in the complex plane parallel to the imaginary axis from $\theta = \pi/2$ to $\theta = \pi/2 - i\infty$. The integrand corresponds to homogeneous plane waves along the real part of the integration path and to inhomogeneous waves radiated parallel to the xy-plane along the complex part. The inhomogeneous waves propagate with a phase velocity of $\alpha' = \alpha/\cosh(\theta_2) < \alpha$ and their amplitudes decay in the vertical direction as $e^{-\sinh\theta_2 |z - z_0|}$.

For a homogeneous medium, the integration over ϕ can be carried out analytically. Eq. (4) then simplifies to Sommerfeld's integral, which represents the spherically symmetric solution of eq. (2) by a superposition of cylindrical elementary waves:

$$\frac{1}{R}\,e^{ikR} = ik \int_0^{\frac{\pi}{2} - i\infty} J_0(kr\sin\theta)\,e^{ik|z - z_0|\cos\theta}\sin\theta\,d\theta\,, \qquad (6)$$

where J_0 is the Bessel function of order zero and $r = \sqrt{x^2 + y^2}$ gives the distance from the source location in the xy-plane.

Homogeneous and inhomogeneous P waves radiated from the point source interact with the free surface. They are partly reflected as P waves and partly converted into S waves. The latter are the focus of our interest. The P-to-S-wave conversion at the free surface obeys Snell's law,

$$p = \frac{\sin\theta}{\alpha} = \frac{\sin\theta_S}{\beta}\,, \qquad (7)$$

where p is the horizontal slowness, θ is the angle of incidence of the P wave (equivalent to the propagation angle used above) and θ_S is the reflection angle of the P-to-S-wave conversion.

In analogy to the incident P wave, the shear potential ψ of the P-to-S-wave conversion at the free surface can be expressed as a superposition of cylindrical waves multiplied by the PS reflection coefficient (Hron & Mikhailenko 1981),

$$\begin{aligned}
\psi(r, z, t) = \frac{1}{2\pi} \int_{-\infty}^{\infty} &e^{-i\alpha kt} \\
\times \int_0^{\frac{\pi}{2} - i\infty} &R_{PS} J_0(kr\sin\theta)\,e^{ik\left(z_0\cos\theta + \frac{z}{\beta}z\cos\theta_S\right)}\sin\theta\,d\theta\,dk.
\end{aligned} \qquad (8)$$

The reflection coefficient is given by

$$R_{PS} = \frac{4\,\dfrac{\cos\theta}{\alpha}\,(\beta^{-2} - 2p^2)}{4p^2\,\dfrac{\cos\theta}{\alpha}\,\dfrac{\cos\theta_S}{\beta} + (\beta^{-2} - 2p^2)^2}\,, \qquad (9)$$

with $\mathscr{Im}(\cos\theta) \geq 0$ for $p > \alpha^{-1}$ and $\mathscr{Im}(\cos\theta_S) \geq 0$ for $p > \beta^{-1}$.

Given the complex-valued angle of incidence $\theta = \theta_1 - i\theta_2$, we can discriminate between three basic regimes.

(1) $\theta_2 = 0$: the angle of incidence θ and the reflection angle θ_S are real-valued. In this case both the incident P wave and the reflected S wave are homogeneous. The reflected S wave corresponds to the geometric P-to-S conversion.

(2) $\theta_1 = \pi/2$, $\theta_2 < \operatorname{arc\,cosh}(\alpha/\beta)$: the incident P wave is inhomogeneous, but the reflected S wave is homogeneous, i.e. θ_S is real-valued. The resulting S waves, i.e. S^* and $\bar{P}S$, are non-geometric.

(3) $\theta_1 = \pi/2$, $\theta_2 > \operatorname{arc\,cosh}(\alpha/\beta)$: both the incident P wave and the reflected S wave are inhomogeneous and therefore confined to the free surface. For a specific value of θ_2 this results in the generation of Rayleigh surface waves.

The generation of S-wave energy at the free surface depends on the magnitude of the reflection coefficient and on the source depth. Computing the shear potential (eq. 8) using the Cagniard–de Hoop method provides insight into the nature of S-wave generation. In the case of a $\delta(t)$ source pulse placed at depth z_0 below the free surface we obtain the proportionality (Hron & Mikhailenko 1981)

$$\psi(r, z, t) \propto \mathscr{Im}\left[R'_{PS}(p)\,\frac{dp}{dt}\right]_{p = p(t)}\,, \qquad (10)$$

with the modified reflection coefficient

$$R'_{PS}(p) = \frac{4p(\beta^{-2} - 2p^2)}{4p^2\xi\eta + (\beta^{-2} - 2p^2)^2} \qquad (11)$$

and the radiation conditions

$$\xi = \sqrt{\alpha^{-2} - p^2} \qquad \mathscr{Re}(\xi) \geq 0\,, \qquad (12)$$

$$\eta = \sqrt{\beta^{-2} - p^2} \qquad \mathscr{Re}(\eta) \geq 0\,. \qquad (13)$$

The shear potential ψ can thus be evaluated by collecting the values of the reflection coefficient R'_{PS} along the Cagniard path $p(t)$ weighted by the time derivative of the path. The Cagniard path is implicitly defined by

$$t = p\sqrt{(z - z_0)^2 + x^2} + z_0\xi + z\eta\,, \qquad (14)$$

where t is the time.

2.2 Results

Here we show the results obtained with the Cagniard–de Hoop method for homogeneous half-space models with different Poisson's ratios. An explosive source emitting a $\delta(t)$-pulse is located at 1 m depth and a single receiver is located at an offset of 10 m. The receiver is located 1 m below the free surface in order to reduce the dominance of the Rayleigh wave. The upper part of Fig. 2 displays the shear potential (eq. 10) for a similarly high Poisson's ratio ($\sigma = 0.498$, $\alpha = 1500$ m s^{-1}, $\beta = 110$ m s^{-1}) to that prevailing in the observed seismic data (Fig. 1). We observe three arrivals: (i) the small peak at $t \approx 16$ ms represents the geometric P-to-S-wave conversion; (ii) the broad pulse with its maximum at $t \approx 52$ ms is the non-geometric P-to-S-wave conversion $\bar{P}S$; (iii) the third peak of the shear potential corresponds to a combination of the non-geometric S^* phase and the Rayleigh wave. Note that for the chosen receiver location, there is interference between the S^* wave and the Rayleigh wave.
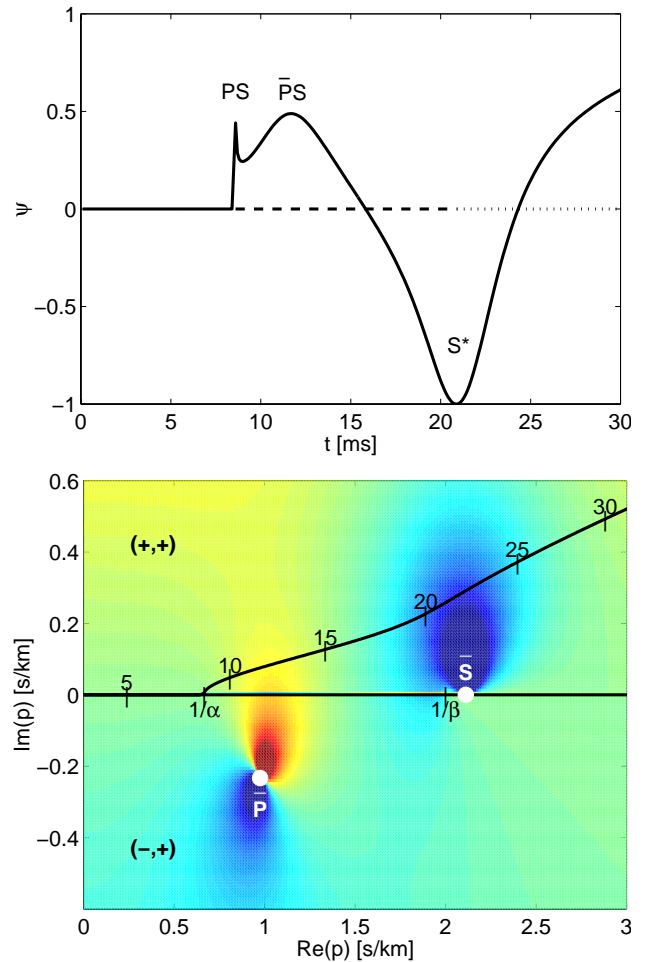
The lower part of Fig. 2 displays the imaginary part of the reflection coefficient $\mathscr{Im}(R'_{PS})$ and the Cagniard path (eq. 14) in the complex p-plane with the traveltime denoted along the path. The Cagniard path follows the real axis until it reaches $p = 1/\alpha$, where the geometric P-to-S-wave conversion makes its contribution to the shear potential. Then the path turns into the first quadrant of the complex p-plane. According to eq. (7), the angle of incidence θ is now complex-valued and we are dealing with the reflection of inhomogeneous P waves. The reflection coefficient is displayed for two different Riemann
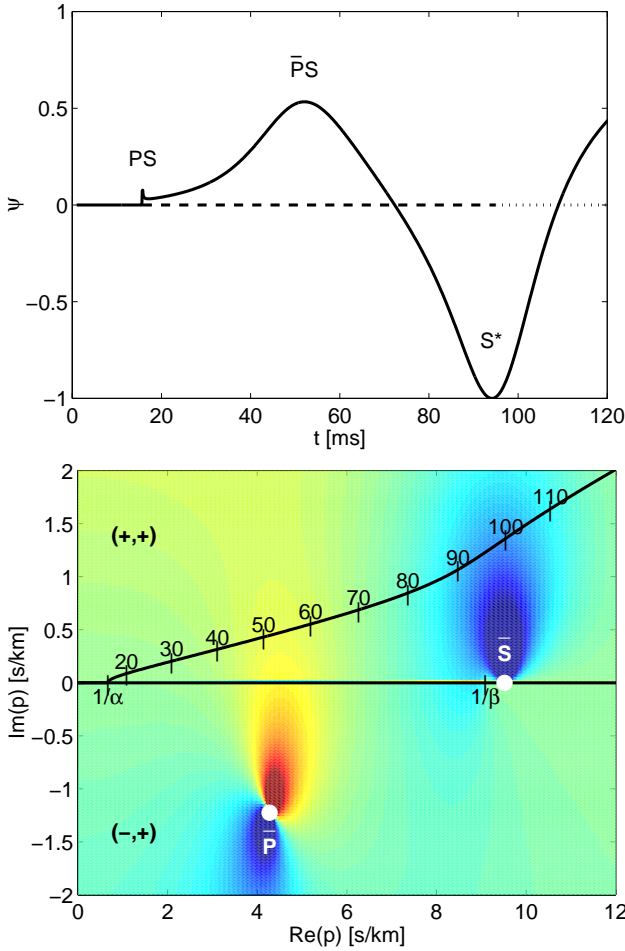
Figure 2. Top: normalized shear potential for $\alpha = 1500$ m s^{-1} and $\beta = 110$ m s^{-1}, i.e. $\sigma = 0.498$. The different types of shear wave regimes are indicated along the time axis (solid: geometric wave; dashed: non-geometric waves; dotted: Rayleigh wave). Bottom: Cagniard–de Hoop path in the complex slowness plane and colour-coded imaginary part of the reflection coefficient $\mathscr{I}m(R'_{PS})$. Positive values are displayed in red and negative values are in blue. For $\mathscr{I}m(p) \geq 0$ the reflection coefficient is shown on the physical Riemann sheet $(+, +)$ and for $\mathscr{I}m(p) < 0$ on the forbidden sheet $(-, +)$.

Figure 3. The same as Fig. 2, but for $\alpha = 1500$ m s^{-1} and $\beta = 500$ m s^{-1}, i.e. $\sigma \approx 0.438$. Note the different scaling of the axes with respect to Fig. 2.

sheets. The range $\mathscr{I}m(p) \geq 0$ shows the reflection coefficient on the physical $(+, +)$ Riemann plane. In this plane, inhomogeneous waves satisfy the radiation condition, that is, they decay exponentially with increasing depth z, and eq. (8) provides stable solutions for the shear potential. For $\mathscr{I}m(p) < 0$ we display the reflection coefficient on the unphysical forbidden Riemann sheet $(-, +)$.
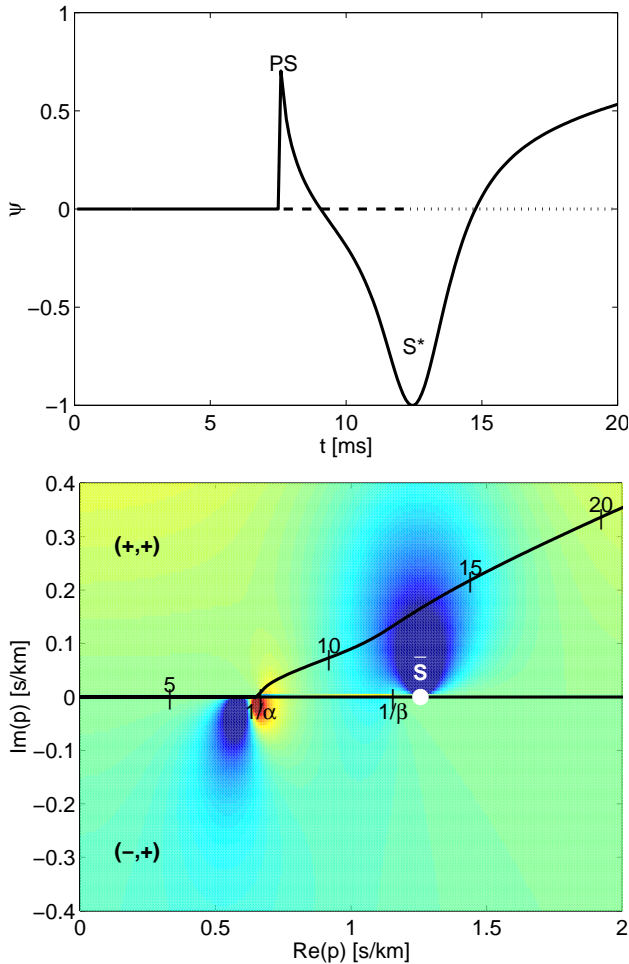
We observe two poles denoted as $\bar{S}$ and $\bar{P}$ (Gilbert *et al.* 1962; Aki & Richards 1980). The $\bar{S}$-pole, or Rayleigh pole, lies on the real p-axis of the physical Riemann plane near the slowness $1/\beta$. This pole gives rise to the Rayleigh surface waves and the non-geometric S^* wave. The $\bar{P}$ pole lies on the forbidden $(-, +)$ sheet almost halfway between $1/\alpha$ and $1/\beta$. Although this pole is on an unphysical Riemann plane, it influences the reflection coefficient on the physical plane. Because of the analytical continuity of the reflection coefficient across the branch cut, the effect of the $\bar{P}$-pole reaches into the physical plane. This results in a contribution to the shear

potential in the form of the $\bar{P}S$ phase if the Cagniard path is close to the real p-axis, that is, when the source and the receiver are close to the free surface. For our source–receiver geometry, the amplitude maximum of the $\bar{P}S$ phase is obtained at a slowness p of about 4.5 s km^{-1}. We can therefore interpret this phase as a reflection of an inhomogeneous P wave propagating parallel to the free surface with a phase velocity of about 220 m s^{-1}.

The position of the $\bar{P}$-pole depends on the Poisson's ratio σ and thus on α/β. With decreasing α/β, the pole moves in the direction of the branch point $1/\alpha$. Fig. 3 shows the results for the same parameters as in Fig. 2 except for a higher shear wave velocity $\beta = 500$ m s^{-1} corresponding to a Poisson's ratio of $\sigma = 0.438$. The proximity of the $\bar{P}$-pole to the branch point $1/\alpha$ has two effects: (i) the non-geometric $\bar{P}S$ phase arrives shortly after the geometric PS phase and (ii) the temporal duration of the $\bar{P}S$ pulse becomes smaller. The maximum amplitudes of the PS and $\bar{P}S$ phases are almost equal. Fig. 4 illustrates the results for $\alpha = 1500$ m s^{-1} and $\beta = 866$ m s^{-1}. This corresponds to a Poisson's ratio $\sigma = 0.25$, which is representative of crystalline rocks. Here the $\bar{P}$-pole lies on the real p-axis near the branch point $1/\alpha$, and hence the $\bar{P}S$ phase does not propagate as a distinct pulse, but interferes with the geometric PS reflection.
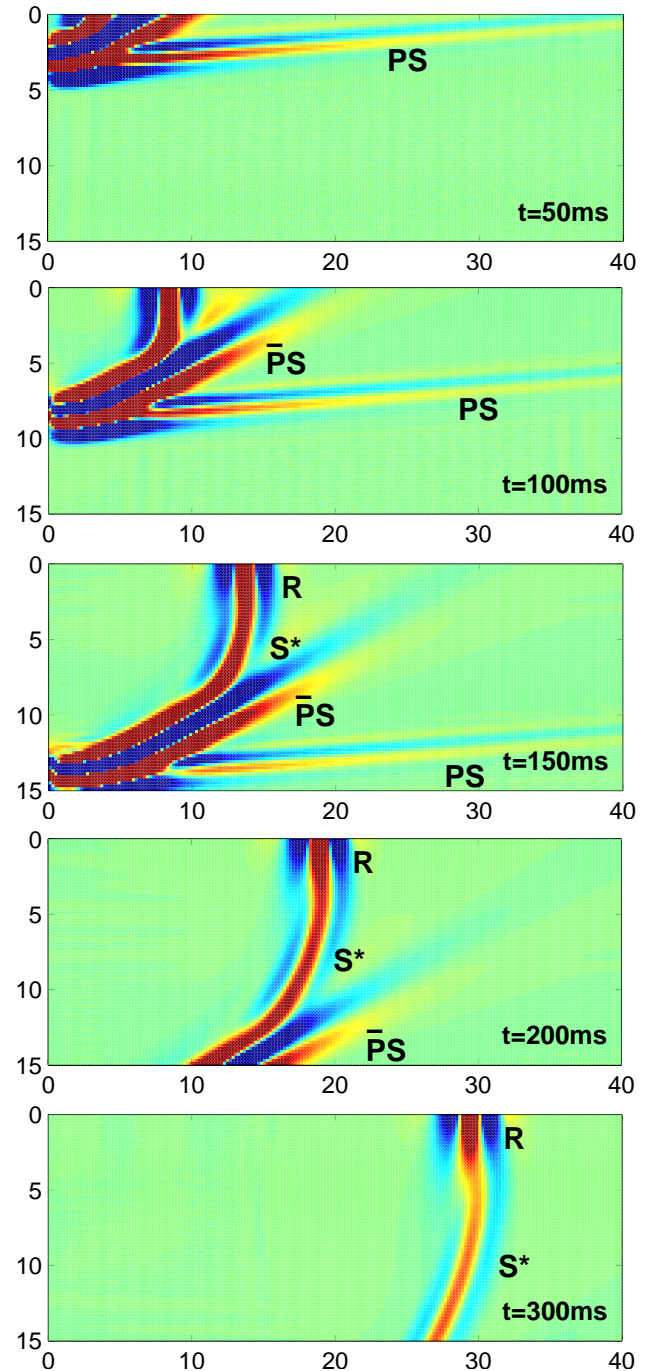
Figure 4. The same as Fig. 2, but for $\alpha = 1500$ m s^{-1} and $\beta = 866$ m s^{-1}, i.e. $\sigma = 0.25$.

Figure 5. Snapshots of the shear wave component of the wavefield (curl) propagating in a homogeneous half-space ($\alpha = 1500$ m s^{-1}, $\beta = 110$ m s^{-1}, $\rho = 1800$ kg m^{-3}). An explosive source close to the surface generates a geometric *P*-to-*S*-wave conversion (*PS*), two non-geometric waves (P̄S and *S**) and the Rayleigh wave (*R*).

3 FINITE DIFFERENCE SIMULATIONS

In order to illustrate the theoretical results derived above, we performed 2-D finite difference simulations assuming a homogeneous half-space with a *P*-wave velocity α of 1500 m s^{-1}, density ρ of 1800 kg m^{-3} and shear wave velocities β of 110 km s^{-1} ($\sigma = 0.498$), 500 m s^{-1} ($\sigma = 0.438$) and 866 m s^{-1} ($\sigma = 0.25$). The model size is 40×20 m, which for the uniform grid spacing of 0.2 m used corresponds to 200×100 gridpoints. The model is surrounded by absorbing boundaries except along the top, where a free-surface boundary condition is applied. An explosive source emitting a 50 Hz Ricker wavelet is placed at 1 m depth at $x = 0$ m.

Fig. 5 shows the snapshots of the shear wave component (curl) of the wavefield propagating through the model characterized by the parameters estimated from the observed seismic data shown in Fig. 1 ($\alpha = 1500$ m s^{-1}, $\beta = 110$ m s^{-1}, $\rho = 1800$ kg m^{-3}). The first snapshot taken after 50 ms shows the geometric *PS* conversion that propagates downwards with the *S*-wave velocity β. This wave can be described by an upward-propagating *P* wave, a conversion at the free surface that obeys Snell's law and a downward-propagating *S* wave. It corresponds to a geometric wave because both the incidence and the reflection angles are real-valued. Since the geometric *PS* conversion is attached to the direct *P* wave and propagates

with it along the free surface, this phase cannot be observed separately in surface seismograms. Note that after 50 ms the direct *P* wave has already travelled over a distance of 75 m. The snapshot at 100 ms clearly shows the non-geometric P̄S wave travelling downwards at an angle of about 30 with respect to the vertical direction. In the snapshots taken after 150 and 200 ms, the well-known non-geometric *S** phase (Hron & Mikhailenko 1981; Dohr 1985) and the Rayleigh wave *R*
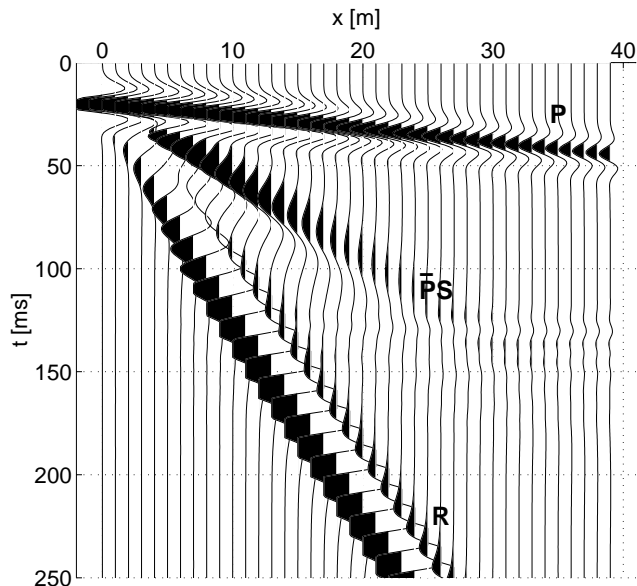
**Figure 6.** Trace-normalized synthetic shot gather for homogeneous half-space model [$\alpha = 1500$ m s^{-1}, $\beta = 110$ m s^{-1} ($\sigma = 0.498$)]. *P*: direct *P* wave; *R*: Rayleigh wave; $\bar{P}S$: non-geometric shear wave.

Figure 7. The same as Fig. 6 but for $\beta = 500$ m s^{-1} ($\sigma = 0.438$).

emerge. *S** propagates radially and seems to arise from the surface location directly above the source point. The *S** phase is difficult to observe at the surface because of its low amplitude at the free surface and because it propagates only slightly faster than the Rayleigh wave and interferes with it at short offsets. Unlike the *S** wave, the non-geometric $\bar{P}S$ wave can be recorded as a distinct phase at the free surface. It does not interfere with other phases and has a high amplitude at short offsets (≤ 20 m). The last snapshot at 300 ms illustrates the decoupling of the Rayleigh wave from the *S** phase.

Fig. 6 shows the resulting synthetic shot gather consisting of the vertical component of the particle velocities recorded at the free surface. It contains three arrivals: the direct *P* wave, the Rayleigh wave and the non-geometric $\bar{P}S$ wave. In agreement with the observed $\bar{P}S$ wave the synthetic $\bar{P}S$ wave has a phase velocity of about 220 m s^{-1}, that is, about twice the *S*-wave velocity at the source location (Gilbert *et al.* 1962), and a similar amplitude-offset behaviour. Figs 7 and 8 show synthetic shot gathers for models with lower Poisson's ratios, $\sigma = 0.438$ and $\sigma = 0.25$, respectively. The time-offset window between the *P* and Rayleigh waves narrows and the $\bar{P}S$ phase interferes with the direct *P* wave at lower Poisson's ratios (Fig. 7). The resulting broadening of the pulse shape of the direct *P* wave for $\sigma = 0.438$ might be misinterpreted as being due to intrinsic attenuation. Interference of the $\bar{P}S$ wave with the direct *P* wave could also result in biased estimates of the *P*-wave velocity in the immediate subsurface, if, as is commonly practiced, the maximum of the first cycle is picked. At a Poisson's ratio typical of crystalline crustal and mantle rocks, i.e. $\sigma = 0.25$, the $\bar{P}S$ phase is no longer apparent in the data (Fig. 8).

4   CONCLUSIONS

In a homogeneous full space, an explosive seismic source radiates only *P* waves. However, if the source is placed near the free surface, some of the *P*-wave energy is converted into shear wave energy. The resulting wavefield consists of geometric,
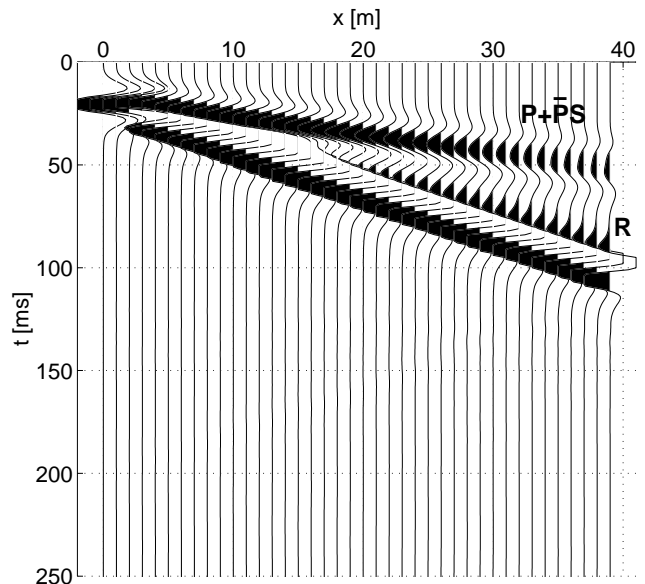
non-geometric and Rayleigh waves. The geometric *PS* phase results from the reflection and conversion of homogeneous plane *P* waves at the free surface. Non-geometric shear waves are due to the conversion of inhomogeneous *P* waves into homogeneous *S* waves, and Rayleigh waves are composed of inhomogeneous *P* waves and their conversion into inhomogeneous *S* waves. In surface seismic measurements Rayleigh waves usually represent the dominant shear wave contribution. The geometric *PS* conversion and the non-geometric *S** wave cannot be observed because they propagate with the direct *P* wave and the Rayleigh wave, respectively. However, for high Poisson's ratios, the source–surface interaction generates an additional non-geometric wave, which can have high amplitudes at near offsets and emerge as a distinct arrival in the shot gather. The non-geometric $\bar{P}S$ wave is particularly relevant
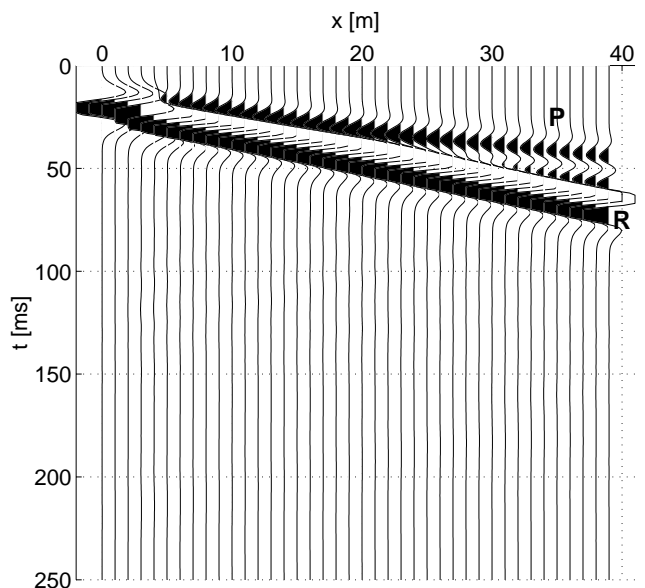
Figure 8. The same as Fig. 6 but for $\beta = 866$ m s^{-1} ($\sigma = 0.25$).

for shallow high-resolution seismic surveys, where very high Poisson's ratios are common. We could identify the $\bar{P}S$ wave clearly in our data set because of the high signal-to-noise ratio of the data and the structural simplicity of the probed site. Under less favourable conditions, the existence of the $\bar{P}S$ phase could remain veiled, or worse, it could lead to misinterpretations if one is not aware of its presence. In general, the $\bar{P}S$ wave increases the complexity of a seismic shot record that could be mistaken as being due to structural heterogeneity of the immediate subsurface. A potential practical application of the $\bar{P}S$ phase may be an independent estimation of the shear wave velocity in the immediate vicinity of the source location.

ACKNOWLEDGMENTS

REFERENCES

Aki, K. & Richards, P.G., 1980. *Quantitative Seismology: Theory and Methods,* W. H. Freeman, San Francisco.

Brekhovskikh, L.M., 1980. *Waves in Layered Media,* Academic Press, New York.

Chapman, C.H., 1972. Lamb's problem and comments on the paper 'On leaking modes' by Usha Gupta, *Pure appl. Geophys.,* **94,** 233–247.

Dohr, G.P., ed., 1985. *Seismic Shear Waves, Part A: Theory, Handbook of Geophysical Exploration,* Vol. 15A, Geophysical Press, London.

Fertig, J., 1984. Shear waves by an explosive point source: the earth surface as a generator of converted *P–S* waves, *Geophys. Prospect.,* **32,** 1–17.

Gilbert, F. & Laster, S.J., 1962. Excitation and propagation of pulses on an interface, *Bull. seism. Soc. Am.,* **52,** 299–319.

Gilbert, F., Laster, S.J., Backus, M.M. & Schell, R., 1962. Observation of pulses on an interface, *Bull. seism. Soc. Am.,* **52,** 847–868.

Gutowski, P.R., Hron, F., Wagner, D.E. & Treitel, S., 1984. *S*, Bull. seism. Soc. Am.,* **74,** 61–78.

Hron, F. & Mikhailenko, B.G., 1981. Numerical modelling of non-geometrical effects by the Alekseev–Mikhailenko method, *Bull. seism. Soc. Am.,* **71,** 1011–1029.

Kisslinger, C., 1959. Observations of the development of Rayleigh-type waves in the vicinity of small explosions, *J. geophys. Res.,* **64,** 429–486.

Kuhn, M.J., 1985. A numerical study of Lamb's problem, *Geophys. Prospect.,* **33,** 1103–1137.

Lash, C.C., 1985. Shear waves produced by explosive sources, *Geophysics,* **50,** 1399–1409.

Leet, L.D., 1949. Earth motion from the atomic bomb test, *Am. Sci.,* **34,** 198–211.

Robertsson, J.O.A., Holliger, K., Green, A.G., Pugin, A. & De Iaco, R., 1996. Effects of near-surface waveguides on shallow high-resolution seismic refraction and reflection data, *Geophys. Res. Lett.,* **23,** 495–498.

Stümpel, H., Kähler, S., Meissner, R. & Milkereit, B., 1984. The use of seismic shear waves and compressional waves for lithological problems of shallow sediments, *Geophys. Prospect.,* **32,** 662–675.

Tsvankin, I., 1995. *Seismic Wavefields in Layered Isotropic Media,* Samizdat Press, Colorado School of Mines, Colorado.